Advances in Water Resources 193 (2024) 104801

Contents lists available at ScienceDirect

Advances in Water Resources

journal homepage: www.elsevier.com/locate/advwatres

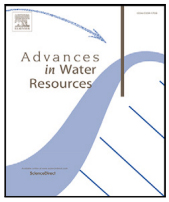

Dam-Break waves over mobile bed

Andrea Del Gaudio [a], Giovanni La Forgia [b,*], Francesco De Paola [a], Cristiana Di Cristo [a], Michele Iervolino [c], Angelo Leopardi [d], Andrea Vacca [a]

[a] DICEA, University of Naples Federico II, Naples, 80125, Italy
[b] Institute of Marine Sciences, National Research Council (ISMAR-CNR), Rome, 00133, Italy
[c] Department of Engineering, University of Campania Luigi Vanvitelli, Aversa, 81031, Italy
[d] DICeM, University of Cassino and Southern Lazio, Cassino, 03043, Italy

ARTICLE INFO

Keywords:
Dam-break waves
Mobile bed
Laboratory experiments
Saint Venant–Exner model

ABSTRACT

Dam-break waves are a major concern for communities and infrastructures in flood-prone areas. The impact of dam-break waves against rigid obstacles after propagation on a mobile bed is lacking both in experimental datasets and in numerical investigations aimed at assessing the capabilities and limitations of available morphodynamic models. To fill these gaps, a novel data set from experiments of dam-break waves propagating over an erodible bottom and impacting over a vertical wall is presented and compared with numerical simulations performed by the Saint Venant–Exner model. First, the effects of bottom mobility are discussed by comparison with the corresponding fixed bed condition. Then, supplementary conditions are investigated for different initial water levels and reservoir lengths. The comparison with the results of the numerical simulation shows that the relatively simple model employed is able to reproduce the general features of the process and the peak impact force with reasonable accuracy.

1. Introduction

Dam-break flows are characterized by strong flow depth and velocity changes and by the presence of wetting and drying fronts, thus representing a typical example of highly unsteady flows. Owing to their characteristics, dam-break waves may mobilize large amounts of sediment even, comparable to the one of the flowing water (Capart, 2000). Moreover, the erosion, the transport, and the deposition of the sediment may directly cause damages to properties and infrastructures which may be even larger than those resulting from the water flood.

Numerous laboratory experiments of dam-break flows over non-erodible bed, are reported in the literature. Dam-break flows of Newtonian and non-Newtonian fluids have been object of several experimental analyses in straight (typically rectangular) channels, and through geometric singularities (such as channel constrictions and bottom sills). Moreover, the wave impact against isolated obstacles (such as walls or vertical columns of various shapes) or multiple obstacles (such as idealized urban areas) has been deeply experimentally investigated. An extensive review of the experimental researches on these topics has been recently provided by Aureli et al. (2023). In such a review, a comprehensive overview of the considered test conditions, of the used measuring techniques along with the collected data is provided. On the other hand, owing to the increased complexity of the involved phenomena, the dynamics of dam-break waves over erodible bottom has not been so deeply experimentally investigated.

The sudden erosional flow initiated by the release of a dam-break wave over a loose sediment bed was theoretically and experimentally studied by Fraccarollo and Capart (2002). The experiments were carried out in horizontal prismatic flumes of rectangular cross-section and the bed material consisted of cylindrical PVC pellets. The validity of the theoretical results, based on the Riemann wave description of erosional dam-break flow, was shown comparing with the measured interface profiles and velocity fields. Leal et al. (2006) performed experiments in straight rectangular flumes in which a sluice gate is rapidly removed, simulating an instantaneous and complete dam failure. Five types of bed material were used. The role that friction and inertia play on the magnitude of dam-break wave-front was put in evidence.

A series of small-scale laboratory experiments of dam-break waves propagating over loose granular beds was provided by Spinewine and Zech (2007). Two bed materials, i.e. sand and Polyvinyl Chloride (PVC), were used. Imaging techniques were employed to identify the characteristic flow regions and to derive full velocity fields. A dam-break flow in a channel where both the bed and the banks are made of uniform erodible material was experimentally studied by Soares-Frazão et al. (2007). The initial channel cross section was of trapezoidal

* Corresponding author.
E-mail address: giovanni.laforgia@cnr.it (G. La Forgia).

https://doi.org/10.1016/j.advwatres.2024.104801
Received 22 March 2024; Received in revised form 31 August 2024; Accepted 31 August 2024
Available online 3 September 2024

shape and the sand was used for both bed and bank. A non-intrusive laser sheet technique was used to measure the shape of the cross sections. Goutiere et al. (2011) carried out experiments of dam-break flow on mobile bed in an abruptly expanding horizontal channel. The bed material consisted of a coarse uniform sand. Measurements of the flow evolution and the final bed topography were obtained using ultrasonic sensors and digital imaging techniques. Experiments of two-dimensional dam-break flows over a mobile bed made of coarse sand were presented by Soares-Frazao et al. (2012) and used as benchmark for blind test simulations used to evaluate the modeling capabilities of different numerical models within the framework of the NSF–PIRE project, entitled "Modelling of Flood Hazards and Geomorphic Impacts of Levee Breach and Dam Failure". The water level evolution at eight gauging points was measured as well as the final bed topography. Spinewine and Capart (2013) performed experiments in a horizontal rectangular flume and sediment bed was composed by either PVC or sand grains. Measurements were realized combining particle tracking velocimetry (PTV) with a novel method of concentration measurement based on recording the penetration depth of a laser light sheet. Wave profiles, velocity maps and detailed measurements of evolving concentration profiles at selected cross-sections were acquired. Dam-break flows over sediment bed under dry and wet downstream conditions were experimentally investigated by Biswal et al. (2018). The experiments were conducted in a straight horizontal rectangular flume and the bed material was sand. Downstream the gate, flow velocity was measured by using Ultrasonic Velocity Profilers and the bed elevation was also acquired at the end of the experiment. For a dam-break flow over a non-cohesive sand bed, Fent et al. (2019) realized detailed velocity measurements both in the clear water layer and in the moving sediment layer. The channel had a rectangular cross section with glass walls to allow optical access to the bed. Finally, Liu et al. (2022) discussed the evolution of bed morphology under 2D dam-break flow by performing a set of laboratory experiments. The tests were carried out in a glass flume with non-uniform fly ash as bed material. The water levels were measured by pressure sensors which were buried under the sediment layer. Furthermore, the bed morphology was acquired using an ultrasonic ranging system.

From the above literature review it follows that although the modifications of the dam-break wave dynamics induced by the presence of erodible bed have been experimentally documented, none of the above contribution has ever addressed the wave interaction with a single or multiple obstacles for mobile bed conditions.

The numerical modeling of dam-break flows over erodible riverbeds has been the focus of several studies, employing various models. The performance of the models has been assessed by comparing the numerical results with the available experimental data. The most widely used model, which is also the simplest one, is the equilibrium model, i.e., the Saint-Venant–Exner model (Graf and Altinakar, 1998). For this kind of model, two types of numerical strategies can be used, i.e., weakly coupled and fully coupled. In the former, the equations are solved using a two-step method (Juez et al., 2014), while in the latter all the equations are simultaneously solved (Soares-Frazão and Zech, 2011). More complex models have been proposed and adopted to simulate dam-break waves in presence of erodible bed. Indeed, single-layer (e.g., Wang et al., 2000), multi-layer (e.g., Swartenbroekx et al., 2013) or multi-phase (e.g., Di Cristo et al., 2016) models have been used to reproduce the features of the dam break-wave detected experimentally. However, all of the above numerical studies did not simulate any interaction of the wave with obstacles. As far as we are aware, only few numerical studies have investigated the dynamics of a dam-break wave, propagating over an erodible bed, in presence of obstacles. Inspired by a fixed-bed study for which extensive experimental and numerical data are available (Aureli et al., 2015), the effects of the obstacle on the changes in the bottom topography were put in evidence by Di Cristo et al. (2020). The numerical study was carried out using a morphodynamic model belonging to the multi-phase class. With reference to the same test-case of Di Cristo et al. (2020), the effects of sediment inertia were investigated by Di Cristo et al. (2021). The study compared the numerical results of fully coupled equilibrium model with those of a multi-phase one. Independently of the sediment inertia, it has been shown that the presence of an erodible bed may alter the force acting on the obstacle, while the presence of the obstacle may strongly modify the morphodynamics of the erodible bed. More recently, Xu et al. (2023) used a two-phase mesh-free method to simulate the impact of dam break wave against a rigid wall in presence of erodible bed. It has been found that the backward-moving wave caused by the wave impact against the wall can scour the sediment close to the wall itself.

It is worth of note that these last three studies could not provide any comparison against experimental data, since the measurements that would have been required to this aim are not available in the literature. Therefore, the above studies do not allow to conclusively assess the reliability of the numerical models in describing the impact dynamics and to predict the force against the obstacles.

The present paper combines experimental and numerical analyses with the aim of contributing to fill the two aforementioned gaps: first, provide a reliable dataset of dam-break wave impacting against obstacles in mobile bed condition; secondly, assess the reliability of the simplest morphodynamical model in predicting the impact dynamics and force. The considered laboratory setting, already used in Del Gaudio et al. (2024) for experiments with the fixed-bed configuration, is a rectangular channel closed downstream by a vertical wall, which constitutes the obstacle hit by the dam-break wave. The bottom is covered with uniformly graded non-cohesive sand. Measurements of flow depth and of the impact force against the wall are presented and compared with the corresponding ones in identical conditions over fixed bed. The presented dataset and discussion is further widened by independently changing the water depth upstream the dam and length of the reservoir in the streamwise direction. From the numerical standpoint, the performance of a fully-coupled equilibrium model in reproducing the main features of the flow dynamics and the impact force against the wall is investigated by direct comparison with the available experiments.

The manuscript is structured as it follows: the laboratory set-up and the numerical methods are described in Section 2, whereas Section 3 discusses the results from both the experimental and the numerical points of view. Finally, conclusion are drawn in Section 4.

2. Materials and methods

2.1. Experimental set-up

We carried out an original set of laboratory experiments at the Hydraulics Lab of the University of Naples "Federico II". The experimental setting consisted of a rectangular Perspex channel, 2.92 m long, 0.4 m wide, and 0.5 m high (Fig. 1a). As indicated in Fig. 1, the reference system has the $\tilde{x}$ axis as the streamwise coordinate, the $\tilde{z}$ axis is vertical, while the $\tilde{y}$ axis is oriented along the spanwise direction.

The channel is divided into two regions by a movable sluice gate: the reservoir on the left-hand side and the floodplain area on the right side, where a $L_5 = 1.36$ m sand bed embankment, whose thickness is $s = 0.04$ m, is placed at $L_4 = 0.015$ m from the gate. The sand bed embankment presents a short ramp ($\theta = 45°$), followed by a $p = 0.025$ m high flat bottom. We used the same sand of the experiments carried out by Di Cristo et al. (2018), with the following characteristics: median diameter $d_{50} = 1.60$ mm, bulk density in air $\rho_s = 2560$ kg m^{-3}, porosity $\phi = 0.47$ and internal friction angle between 37° and 41°. The sediment grain size was carefully selected in order to adopt the smallest non-cohesive sediment that could be mobilized by the flow resulting from the dam break. As shown in the following Sections, the sand layer is weakly eroded and shaped by the flow except that close to the original position of the dam. We clarify that this is not a limitation of present

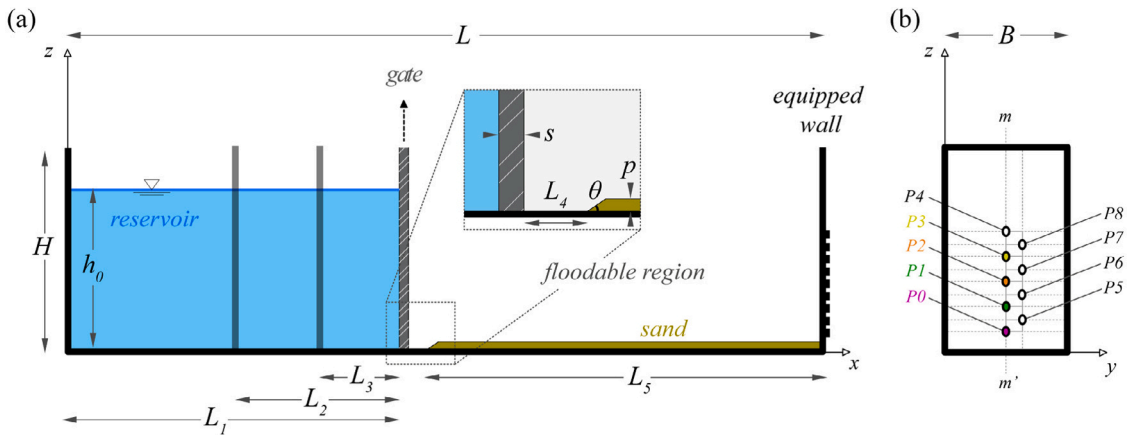

Fig. 1. Sketch of the channel. (a) Lateral view ($x-z$ plane). (b) Frontal view of the downstream wall ($y-z$ plane), equipped with pressure transducers (P_i) distributed in 9 nodes of a lattice composed by 9 × 4 lines spaced 0.02 m along both y and z directions. Transducer P_0 is placed at 0.01 m from the bottom along the wall centerline ($m-m'$).

study, since the comparison of different test case is made considering the same availability of granular material.

Before each experiments, the embankment was saturated with water. A full-width rigid wall is placed at the end of the channel. The reservoir was filled with water, and the final water level h_0 was measured using a hydrometric rod. Three different initial conditions, i.e.: h_0 = 0.16 m, 0.2 m and 0.24 m have been considered. We investigated three different reservoir lengths, by changing the distance of the upstream wall to the lift gate: L_1 = 1.50 m, L_2 = 0.75 m and L_3 = 0.50 m. For the experiments with L_1, we used both the sand embankment and a rigid one, in order to investigate the influence of a movable bed on the dynamic of the dam-break wave and on the extent force on the endwall.

The dam-break wave develops as a pneumatic system suddenly lifts the gate. The lifting velocity of about 1.35 m s^{-1}, allows the removal of the dam in a time, t_R, which has been compared with the characteristic scale t_C (Lauber and Hager, 1998), defined as:

$$t_C = \sqrt{\frac{2h_0}{g}}, \tag{1}$$

where g is the gravity. For all the runs $t_R < t_C$, such that the gate removal may be considered as instantaneous (Lauber and Hager, 1998).

Each experiment was recorded by two high-speed CCD cameras (Iron 250 Kaya Instruments) with a resolution of 5 MegaPixels. The cameras were horizontally aligned and placed perpendicularly to the channel in front of the gate and the downstream vertical end wall. A digital video recording software (Norpix StreamPix) was used to control and synchronize the CCD cameras. The post-processing of the two synchronous frames (performed by MATLAB Toolbox (Zh, 2000) and MATLAB stereo camera calibrator (Heikkila and Silvén, 1997)) allowed to obtain, for each time step, a unique, referenced image devoid of focal distortion. Using image analysis, the instantaneous free surface profiles were obtained.

The vertical wall at the downstream end of the channel was equipped with 9 Gefran TSA pressure transducers (P_i) (Fig. 1b). As indicated in Fig. 1, five transducers, P_0 to P_4, are vertically spaced with a 0.02 m interval along the channel centerline, with P_0 at 0.01 m above the bottom. The transducers P_5 to P_8 are vertically distributed with the same 0.02 m spacing on the right of the centerline. Each transducer can sample pressures with a maximum frequency of 2000 Hz and an accuracy of 0.5% on the full-scale output (0.1 bar). A data acquisition system (Labjack T7) reads and converts the resulting samples into digital values that are analyzed with MATLAB (The MathWorks Inc., 2022). Each transducer was calibrated under hydrostatic conditions. Cameras and transducers were synchronized with the computer timeline and their acquisition frequency was set at 100 Hz.

The instantaneous impact force on the end-wall induced by the dam-break wave was evaluated by integrating on the vertical axis the pressures measured by the centerline transducers, assigning to each one the corresponding influence area of a B × 2 cm stripe. The experimental repeatability has been verified for tests with L_1 = 1.50 m by performing 5 times the experiment for the same experimental condition. The RMS (Root mean square) of the pressure and force measurements cases are about 4% and 3.7%, respectively for fix bed cases and 6% and 5.6% for mobile bed ones. The relative predicted accuracy of the peak force values were 5.0%, 5.1%, 5.2% for the fixed bed for h_0 = 0.16 m, 0.20 m and 0.24 m, respectively; whereas for the mobile bed the corresponding values were 6.9%, 7.0%, 4.0% for h_0 = 0.16 m, 0.20 m and 0.24 m, respectively.

2.2. Numerical model

The Saint-Venant–Exner model (SVE) is derived under the shallow-water assumption by depth-averaging the three-dimensional Reynolds-averaged Navier–Stokes equations The integration assumes pressure distribution as hydrostatic, and unitary value of the momentum correction coefficient. The Saint-Venant–Exner equations read (Graf and Altinakar, 1998):

$$\frac{\partial \tilde{h}}{\partial \tilde{t}} + \frac{\partial \tilde{q}}{\partial \tilde{x}} = 0 \tag{2}$$

$$\frac{\partial \tilde{q}}{\partial \tilde{t}} + \frac{\partial}{\partial \tilde{x}}\left(\frac{\tilde{q}^2}{\tilde{h}} + \frac{g\tilde{h}^2}{2}\right) + \frac{\partial \tilde{z}_b}{\partial \tilde{x}} = -\frac{\tilde{\tau}_b}{\rho} \tag{3}$$

$$(1-\phi)\frac{\partial \tilde{z}_b}{\partial \tilde{t}} + \frac{\partial \tilde{q}_s}{\partial \tilde{x}} = 0 \tag{4}$$

where $\tilde{t}$ denotes the time and $\tilde{x}$ the horizontal coordinate, $\tilde{h}$ the flow depth, $\tilde{z}_b$ the bottom elevation, respectively. In (3), g represents the gravity acceleration, ρ is the liquid density and $\tilde{q}$ (resp. $\tilde{q}_s$) is the liquid (resp. solid) flow rate (per unit width). In what follows, the Chezy formula is used to express the bed shear stress ($\tilde{\tau}_b$) as:

$$\tilde{\tau}_b = \rho\frac{\tilde{q}^2}{C_h^2\tilde{h}^2}, \tag{5}$$

where C_h is the dimensionless Chezy coefficient. Under the customary equilibrium hypothesis, the solid flow rate in Eq. (4) immediately adapts to the transport capacity of the uniform flow under the shear stress $\tilde{\tau}_b$, which is evaluated through the Meyer–Peter and Müller formula (Meyer-Peter and Müller, 1948):

$$\frac{\tilde{q}_s}{d\sqrt{gdr}} = K_{MPM}\left(\frac{\tilde{\tau}_b - \tilde{\tau}_c}{\rho g d r}\right)^{\frac{3}{2}}, \tag{6}$$

where $r = (\rho_s - \rho)/\rho$, d the sediment particle diameter and $\tilde{\tau}_c$ the threshold shear stress for particle motion. The Meyer–Peter and Müller coefficient (K_{MPM}) was originally estimated as $K_{MPM} = 8$.

Cordier et al. (2011) have shown that the PDEs system (2)–(4), whenever a formula such as the Meyer–Peter and Müller equation (Eq. (6)) is used for the bed-load discharge, has a hyperbolic nature. The corresponding eigenvalues are the solutions of the following equation (Carraro et al., 2018):

$$\left(\frac{\tilde{\lambda}}{\tilde{c}}\right)^3 - 2\mathrm{F}\left(\frac{\tilde{\lambda}}{\tilde{c}}\right)^2 - \left(1 - \mathrm{F}^2 + \frac{1}{1-\phi}\frac{\partial \tilde{q}_s}{\partial \tilde{q}}\right)\left(\frac{\tilde{\lambda}}{\tilde{c}}\right) - \frac{1}{1-\phi}\frac{\partial \tilde{q}_s}{\partial \tilde{h}}\frac{1}{\tilde{c}} = 0, \quad (7)$$

where $c = \sqrt{g\tilde{h}}$ and $\mathrm{F} = \frac{\tilde{q}}{\tilde{h}\tilde{c}}$ denotes the Froude number. The roots of Eq. (7) easily follow from the Cardano's formula, and they read:

$$\frac{\tilde{\lambda}_1}{\tilde{c}} = \frac{2}{3}\left[\mathrm{F} - \sqrt{k'}\cos\left(\frac{\psi - \pi}{3}\right)\right] \quad (8)$$

$$\frac{\tilde{\lambda}_2}{\tilde{c}} = \frac{2}{3}\left[\mathrm{F} - \sqrt{k'}\cos\left(\frac{\psi + \pi}{3}\right)\right] \quad (9)$$

$$\frac{\tilde{\lambda}_3}{\tilde{c}} = \frac{2}{3}\left[\mathrm{F} + \sqrt{k'}\cos\left(\frac{\psi}{3}\right)\right] \quad (10)$$

where:

$$\psi = \arccos\left(\frac{k''}{\sqrt{4k'}}\right) \quad (11)$$

$$k' = 3\left(1 + \frac{1}{1-\phi}\frac{\partial \tilde{q}_s}{\partial \tilde{q}}\right) + \mathrm{F}^2 \quad (12)$$

$$k'' = -2\mathrm{F}^3 + 18\mathrm{F}\left(1 + \frac{1}{1-\phi}\frac{\partial q_s}{\partial q}\right) + \frac{27}{\tilde{c}}\frac{1}{1-\phi}\frac{\partial \tilde{q}_s}{\partial \tilde{h}}. \quad (13)$$

In what follows, Eqs. (2)–(4) have been numerically solved with the method described by Di Cristo et al. (2018), as a degenerated case of the general 2D unstructured quadrilateral meshes therein considered. A mixed cell-centered (CCFV) and node-centered (NCFV) finite-volume discretization is considered, with the former adopted for the hydrodynamic variables $\tilde{h}$ and $\tilde{q}$, defined at the grid cell centers, whereas the latter applies to the bed elevation $\tilde{z}_b$. The corresponding control volumes are constructed around the mesh nodes by the median-dual partition (Barth and Jespersen, 1989; Nikolos and Delis, 2009). The first-order Harten–Lax–Van Leer (HLL) scheme (Amiram Harten and Leer, 1983), with second-order reconstruction of the free-surface elevation for subcritical flow (Di Cristo et al., 2018) is employed to compute the numerical fluxes in the CCFV discretization. The eigenvalues of the problem are given by Eqs. (8)–(13). Owing to the hyperbolic character of the problem, the numerical stability of the solution is ensured provided that the Courant–Friedrichs–Lewy condition is satisfied for the largest eigenvalue. Finally, the slope source term in (3) is treated as proposed by Greco et al. (2008) to ensure the satisfaction of the C-property.

Numerical integration has been performed with a timestep $\Delta\tilde{t} = 1/2048$ s and a spatial step $\Delta\tilde{x} = 5 \cdot 10^{-3}$ m. Two values of the dimensionless Chezy coefficient have been considered, one for the smoother non-erodible bottom ($C_h = 22$) and one for the coarser sediment-covered bottom ($C_h = 12$). These values have been chosen by fitting the simulated wave tip celerities to the corresponding experimental values. An a-posteriori analysis confirmed that the considered C_h values are consistent with those predicted by widely used resistance laws for moderate depth-to-grain size ratio i.e., below 100 (e.g., see Fig. 4 in Yadav et al., 2022).

The simulations have been carried out by setting the physical properties of the sediment equal to the corresponding measured values and assuming $d = d_{50}$ and $\tilde{\tau}_c = 0.047\ \rho g d r$.

3. Results

All the experimental tests both in fixed and mobile bed conditions have been numerically reproduced. The force acting at the centerline of the wall ($\tilde{F}$) is estimated by integrating the instantaneous pressure ($\tilde{P}$) distribution derived numerically, in order to compare it with the measured value. In presenting the results, the following dimensionless variables are introduced:

$$t = \frac{\tilde{t}}{t_c},\ z = \frac{\tilde{z}}{h_0},\ x = \frac{\tilde{x}}{h_0},\ v = \frac{\tilde{v}}{(gh_0)^{0.5}},\ P = \frac{\tilde{P}}{P_c},\ F = \frac{\tilde{F}}{F_c}, \quad (14)$$

where t_c is defined by Eq. (1), $P_c = \gamma h_0$ with $\gamma = 9810\mathrm{Nm}^{--3}$ the specific weight of water, $F_c = 0.5\gamma h_0^2$, and $\tilde{v}$ denotes the front celerity.

3.1. Mobile and fixed bed tests: experiments and simulations

This paragraph discusses the effect of the mobile embankment on the dam-break wave propagation and on its interaction with the vertical end wall, along with the ability of the SVE model to reproduce the phenomenon.

Fig. 2 shows the measured and computed free-surface profile along the channel at times ranging between $t = 4.8$, when water surge is propagating in the channel, and $t = 18.8$ when the dam-break wave is almost completely reflected, for both fixed bed (LabExp–FB) and mobile bed experiments (LabExp–MB). Moreover, for all performed tests Fig. 3 depicts the time evolution of the measured pressure at the transducers P_0 and P_1, while Fig. 4 shows the time evolution of the measured force, and the comparison with the corresponding numerical predictions.

Let us first discuss the process dynamics as it appears from the experiments.

In the case of fixed bed, after the gate removal the wave propagates with a front celerity of about $v = 1.78$ until it reaches the end wall at $t = 5$ (Fig. 3b). For the mobile bed configuration, the shape of the embankment is suddenly altered in consequence of the surge transit. After this phase, the surge propagates on the embankment at an almost constant front celerity of about $v = 1.07$ and it reaches the end wall at $t = 6.43$, about $t = 1.43$ later than the LabExp–FB. After colliding with the obstacle, the wave forms a vertical jet that runs-up the wall. For LabExp–FB, the jet forms a 90° angle with the incoming water until it reaches the maximum run-up height at $t = 7.1$ (Fig. 2c). At the wave arrival, the transducer closest to the bottom (i.e., P_0) measures a single impulsive pressure increase (Fig. 3b), corresponding to a sudden growth of the force (Fig. 4b). Later on, a counter clock-wise vortex forms due to the falling jet, causing the entertainment of a large quantity of air (Fig. 2e,g) which produces oscillations and irregular pulsations of the pressure (Fig. 3b). Successively, due to the further income of water, the force increases (Fig. 4b) until it reaches the maximum value when the water level on the wall is maximum and the front of the backward propagating bore is in the middle of the floodable area (Fig. 2g). It is worth of remark that this phase is characterized by a nearly hydrostatic distribution of the pressures acting over the wall and by the release of downstream-propagating Favre waves (Del Gaudio et al., 2024).

In mobile bed conditions, sediment entrained by the wave front deposits close to the end wall forming a more gradual pathway for the jet impact (Fig. 2f). The maximum run-up height is reached at $t = 10$, then, the counter clock-wise vortex develops (Fig. 2h). Since some flow momentum is likely to be transferred to sustain the bed-load transport, the flow impact on the wall is less impulsive, as indicated by the pressure signal of the P_0 transducer, which does not show the aforementioned peak (Fig. 3b) and presents less oscillations than LabExp–FB. This corresponds to monotone and less steep increment of the force (Fig. 4b).

In terms of bed evolution, in the first part of the embankment 2-D bed forms are present (Fig. 2d, f, h, l), while an irregular pattern is formed on the bottom close to the wall, due to the presence of

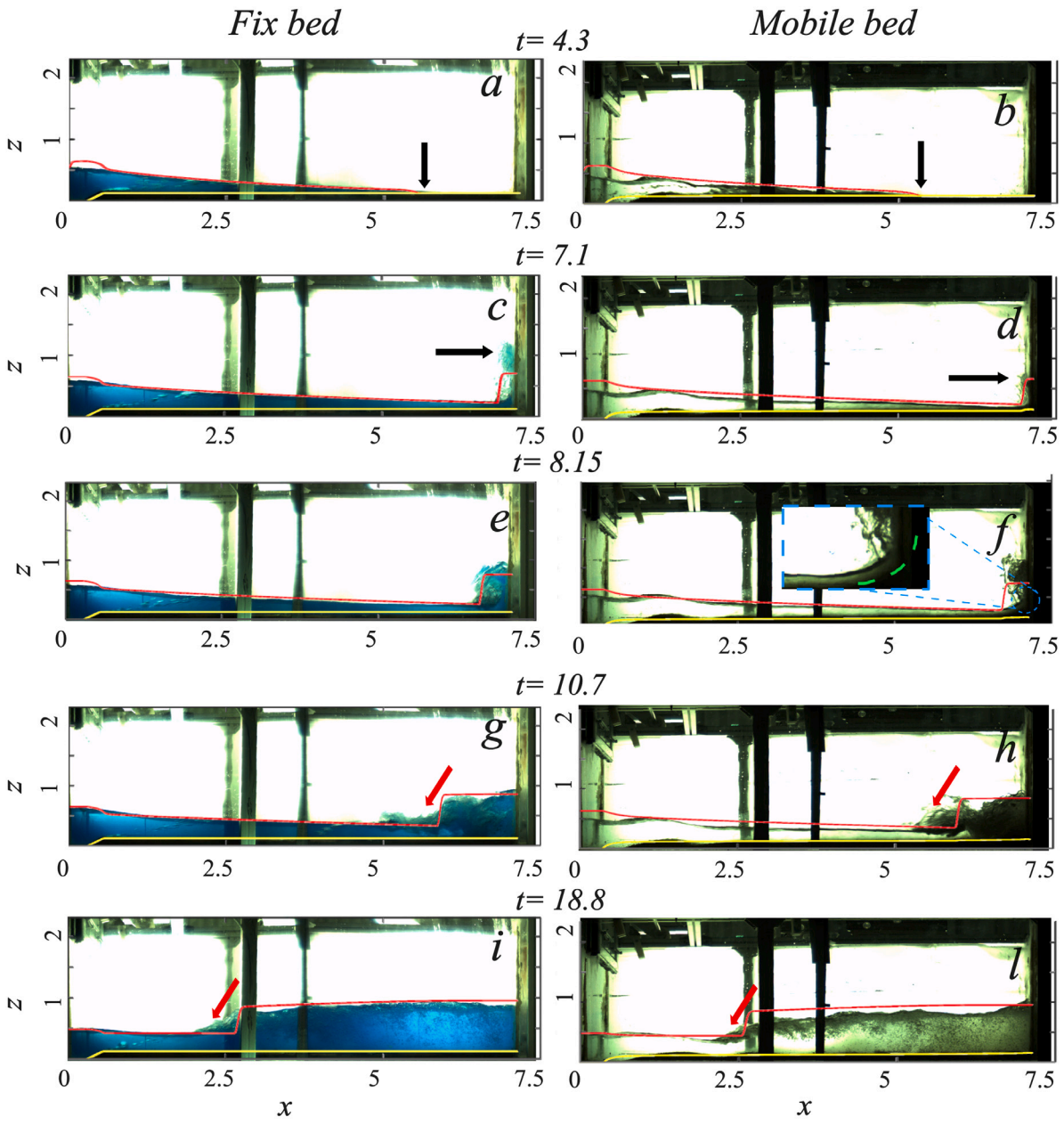

Fig. 2. Flow depth profiles for $h_0 = 0.2$ m at different instants. LabExp–FB (left panels), LabExp–MB (right panels). Red lines: simulated free surface; yellow lines: simulated bed profile. Black arrows show the front position of the surge. Red arrows show the front position of the propagating bore. For the fixed-bed case, Methylene blue was dissolved into the water to improve image readability.

the vortex during the early stage of the impact. The bed modification influences the free surface, that shows a more undulated profile than the LabExp–FB.

After the impact phase ($t > 10$) the differences between the fixed and mobile bed cases are smaller (Fig. 3b, Fig. 4b). For the LabExp–MB, the force time series shows slightly higher values (Fig. 4b). It could be hypothesized that this relatively small increase of the force in the nearly hydrostatic phase is due to a reduction of the overall bottom resistance resulting from the previous morphodynamical changes in the embankment shape.

The other two cases behave similarly to the $h_0 = 0.2$ m one, under both fixed and mobile bed conditions. Results show that the differences between LabExp–FB and LabExp–MB tests, in terms of wave arrival time to the end wall and maximum force values, decrease with the initial water depth (Figs. 3 and 4). In particular, the shift in the arrival time are $t = 3, 1.5, 0.9$ and percentage differences of peak force values are 9.3%, 6.5%, 5.0% for $h_0 = 0.16$ m, 0.20 m and 0.24 m, respectively. This behavior may be attributed to the reduction of the mobile bed embankment influence as the p/h_0 ratio decreases.

Let us now focus on the reproduction of the process dynamics by the SVE model. It is expected that since the SVE model assumes negligible vertical accelerations, several flow features of the wave–structure interaction which were observed experimentally could not be captured. For instance, the SVE simulations cannot capture the formation of vortexes in the vertical plane nor air entertainment from the free-surface. This notwithstanding, there is still room for understanding to what extent the SVE model, despite its limitations, may reproduce some relevant aspects of this complex process, such as the time development of the impact force, its peak value and the embankment morphodymanics. In what follows, results from the fixed and mobile bed simulations are denoted as SVE–FB and SVE–MB, respectively.

Fig. 4 reports the comparison of the time evolution of the measure dimensionless impacts forces with the prediction of the SVE–FB and

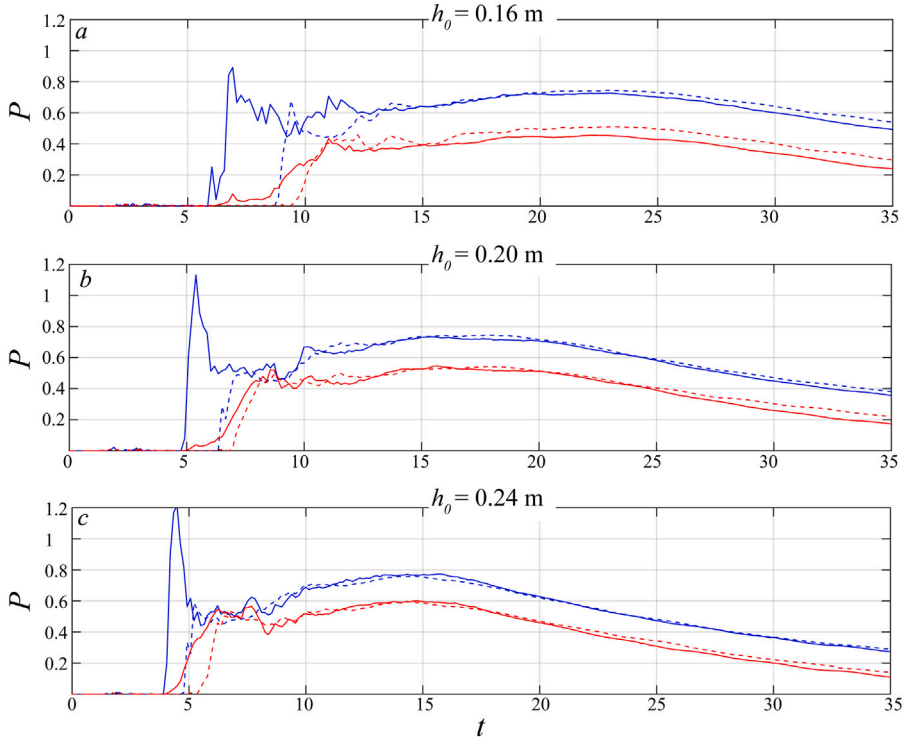

Fig. 3. Time histories of non-dimensional pressure measured by P_0 (solid blue line, fixed bed and, dashed blue line, mobile bed) and P_1 (solid red line, fixed bed and, dashed red line, mobile bed) transducers, (a) $h_0 = 0.16$ m, (b) $h_0 = 0.20$ m, (c) $h_0 = 0.24$ m.

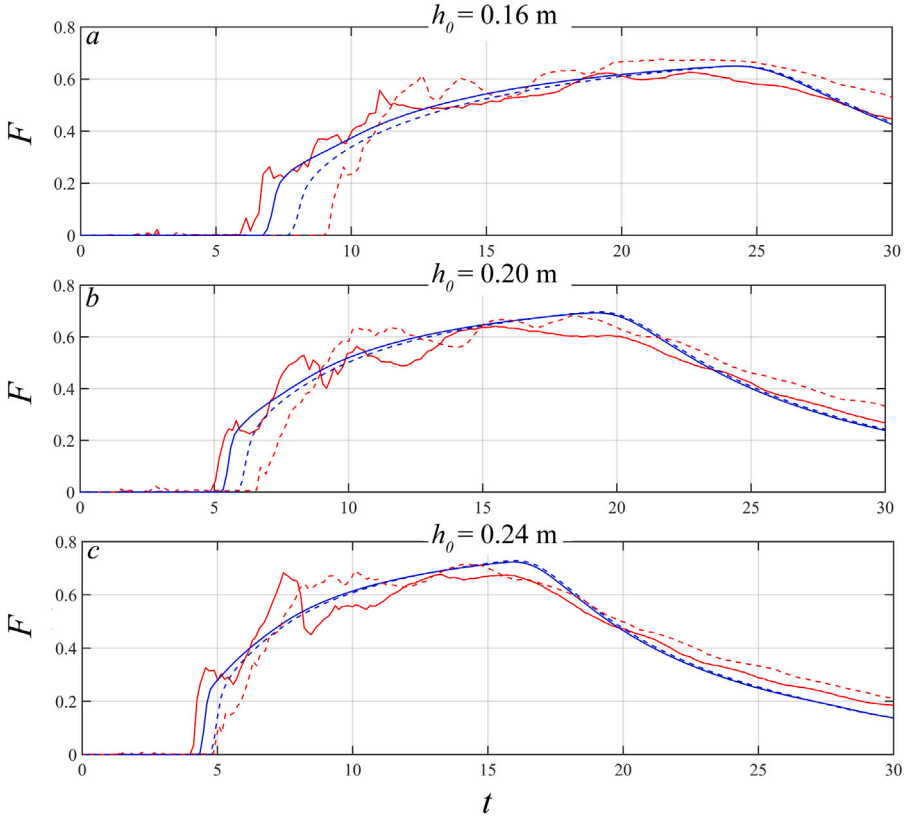

Fig. 4. Time histories of the non-dimensional impact force for case (a) h_0 = 0.16 m, (b) h_0 = 0.2 m and (c) h_0 = 0.24 m. Experimental results LabExp–FB (solid red lines) and LabExp–MB (dashed red lines) and SVE–FB (solid blue lines) and SVE–MB (dashed blue lines) numerical simulations.

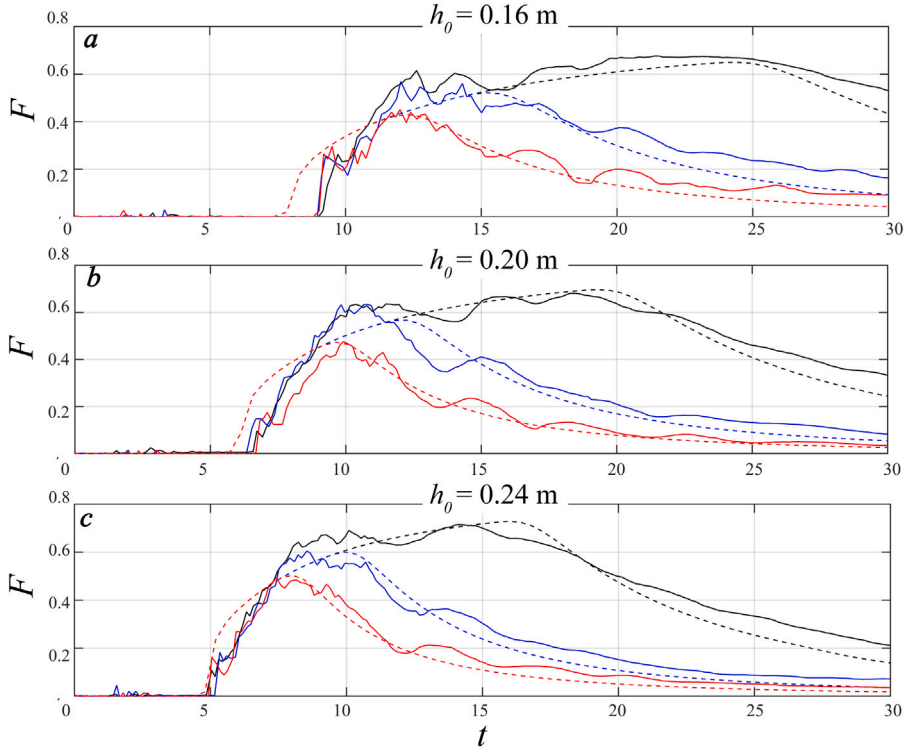

Fig. 5. Time history of the non-dimensional impact force for different reservoir lengths for case (a) h_0 = 0.16 m, (b) h_0 = 0.2 m and (c) h_0 = 0.24 m. Experimental results LabExp–MB–L1 (solid red lines), LabExp–MB–L2 (solid blue lines) and LabExp–MB–L3 (solid black lines) are compared with those derived from the SVE–MB model (dashed lines).

SVE–MB simulations. The model qualitatively reproduces the shift in the arrival time of the surge at the endwall between the fixed and mobile conditions. However, there is a systematic underestimation of the temporal shift, larger for lower h_0 values. In fact, when the ratio among the embankment height and the initial water depth increases, the vertical accelerations become more prominent when the surge impacts against the embankment, with a consequent worse agreement of the SVE simulated results.

The SVE simulations predict a monotonic increase of the force until the maximum value is reached, without reproducing the oscillatory behavior observed in the experiments. The maximum force value is reached slightly later than in the experiments and the same values are predicted by the fixed and mobile bed cases. The error on the prediction of the measured maximum impact force is less than 10% respect both mobile and fixed bed cases.

3.2. Effect of the reservoir length

Additional experiments with mobile bed were carried out by varying the length of the reservoir aiming to assess the influence of this parameter on the impact force on the vertical wall, to extend the experimental dataset and to perform wider benchmark conditions for the SVE models. Specifically, for each initial water level h_0, we considered the three different reservoir lengths reported in the setup description (i.e., L_i, with $i = 1, 2, 3$ in Fig. 1). Consistently with the previous analysis, the measured time evolution of dimensionless impact forces are compared with those obtained from the SVE–MB model in Fig. 5.

Changing the reservoir length at constant h_0 does not affect the wave propagation phase after the gate removal. The waves reach the vertical wall approximately at the same dimensionless time (e.g., at $t \simeq 8$ for $h_0 = 0.20$ m, in Fig. 5b). The wave propagation speed, indeed, mostly depends on the initial water depth, i.e., on the potential energy of the released fluid.

As described in the previous section, the inertial forces still dominate when the dam-break wave impacts against the wall and a vertical jet forms running up on the end wall. During this phase there is no appreciable effect of the reservoir length and the measured time histories of the forces nearly superpose, for all the considered h_0 values. However, the duration of this phase, in which the impact force progressively grows, increases with the reservoir length. Correspondingly, for each h_0, the force reached at the end of this phase also increases with the reservoir length (Fig. 5). For cases LabExp–MB–L3 and LabExp–MB–L2 the force values reached at the end of the inertial phase also represent the absolute maxima during the entire experiment. After the inertial phase, a quasi–hydrostatic stage follows, during which a nearly hydrostatic distribution of the pressure occurs at the end wall (Del Gaudio et al., 2024). During this quasi–hydrostatic phase, cases LabExp–MB–L1 reach the absolute maxima (see black lines in Fig. 5).

The numerical simulations reasonably reproduce the general trend of the experiments. Specifically, the SVE–MB model is able to capture the two interrelated effects of the increasing reservoir length: the increase of the force peak and the time shift. In particular, the peak force is better reproduced for cases LabExp–MB–L1, where it occurs during the quasi–hydrostatic phase. As expected, the SVE–MB model under-performs when the peak force is attained during the inertial phase, characterized by non-hydrostatic pressure distribution at the end-wall. In fact, for the lower reservoir length values, L_2 and L_3, the simulations show a progressive shift in the time of the peak force occurrence respect to the experimental value. This shift increases as the initial water depth decreases, maybe due to an increase of the influence of the embankment height for the combined effect of a lower h_0 and a smaller volume. Indeed, along with the increase of $\frac{p}{h_0}$, the faster decay of the flow depths consequent to the smaller reservoir length further contributes to a more pronounced deviation from the assumption of a nearly-horizontal shallow flow. Despite this intrinsic limitation, the comparison of the measured and simulated peak impact forces shows that the SVE–MB model is still characterized by an accuracy of less than 10%. It is therefore to be concluded that under the investigated conditions both experiments and numerical simulations

suggest that the reservoir length considerably affects the interaction of the dam-break waves with the end wall, primarily in terms of peak values and temporal evolution of the impact force. The key mechanism can be summarized as follows: the peak force is attained during the quasi-hydrostatic phase, unless the emptying of the reservoir does not significantly reduces the momentum of the incoming wave at the impact. Conversely, the peak force is associated to the inertial phase in which the incident wave runs up the end wall.

4. Conclusions

A novel series of laboratory experiments have been designed and performed to examine the impact of dam-break waves on a vertical wall under both mobile and fixed bed conditions. To the authors' knowledge, this experimental analysis of the impact force evolution under both conditions is unprecedented in the literature. The same experiments have been also reproduced through the Saint Venant–Exner model in order to evaluate its effectiveness in predicting impact force dynamics. Additional experiments explored the effect of reservoir length in mobile bed conditions.

In the presence of a mobile bed, as expected, the wave dissipates more energy during propagation compared to the fixed bed configuration, resulting in a longer propagation time. Sediment transport develops unevenly along the embankment, generating both depositional and erosional regions. The sediments accumulated close to the vertical wall forms a curved ramp which leads the impinging wave to induce less pronounced oscillations in the impact force, compared to the fixed bed configuration. Our results show a slightly higher peak of the impact force occurring under mobile bed conditions. This counterintuitive finding is related to the induced mobilitation of sand particles during wave propagation, which modify the bed shape.

The length of the reservoir crucially affects the impact force dynamics. For sufficiently long reservoir, the peak impact force is reached during the quasi-hydrostatic phase. Conversely, for shorter reservoirs, it occurs during the inertial phase. The Saint Venant–Exner (SVE) numerical model reasonably predicts the overall behavior of the dam-break phenomenon during both propagation over the mobile bed and the impact phases, with an error in peak impact force estimation below 10%, regardless of reservoir length. However, the numerical simulations better align with the experimental results when the peak of the impact force occurs during the quasi-hydrostatic phase.

These findings suggest several new avenues for investigating the interaction of dam-break waves with physical obstacles in the presence of an erodible bed, which can alter the impact process and potentially lead to more severe damage.

CRediT authorship contribution statement

Andrea Del Gaudio: Writing – original draft, Resources, Methodology, Investigation, Formal analysis, Data curation, Conceptualization. **Giovanni La Forgia:** Writing – original draft, Resources, Methodology, Investigation, Formal analysis, Data curation, Conceptualization. **Francesco De Paola:** Writing – review & editing, Methodology, Funding acquisition. **Cristiana Di Cristo:** Writing – review & editing, Supervision, Resources, Methodology, Investigation, Conceptualization. **Michele Iervolino:** Writing – review & editing, Validation, Supervision, Investigation, Formal analysis, Data curation, Conceptualization. **Angelo Leopardi:** Writing – review & editing, Supervision, Funding acquisition, Conceptualization. **Andrea Vacca:** Writing – review & editing, Supervision, Resources, Methodology, Investigation, Conceptualization.

Declaration of competing interest

The authors declare that they have no known competing financial interests or personal relationships that could have appeared to influence the work reported in this paper.

Data availability

Data will be made available on request.

Acknowledgment

La Forgia, G. was partially supported by the project "Solid transport in rivers and morphodynamic equilibrium of the coasts" (TRASFLUV), financed by Lazio Region, Italy.

References

Amiram Harten, P.D.L., Leer, B.V., 1983. On upstream differencing and Godunov-type schemes for hyperbolic conservation laws. SIAM Rev. 25, 35–61.
Aureli, F., Dazzi, S., Maranzoni, A., Mignosa, P., Vacondio, R., 2015. Experimental and numerical evaluation of the force due to the impact of a dam-break wave on a structure. Adv. Water Resour. 76, 29–42.
Aureli, F., Maranzoni, A., Petaccia, G., Soares-Frazão, S., 2023. Review of experimental investigations of dam-break flows over fixed bottom. Water 15, 1229.
Barth, T., Jespersen, D., 1989. The design and application of upwind schemes on unstructured meshes. In: Proceedings of the 27th Aerospace Sciences Meeting. In: AIAA, American Institute of Aeronautics and Astronautics, Reno, USA.
Biswal, S., Moharana, M., Agrawal, A., 2018. Effects of initial stage of dam-break flows on sediment transport. Sādhanā 43, 1–12.
Capart, H., 2000. Dam-break Induced Geomorphic Flows (Ph.D. thesis). Université Catholique de Louvain, Louvain-la-Neuve, Belgium.
Carraro, F., Valiani, A., Caleffi, V., 2018. Efficient analytical implementation of the DOT Riemann solver for the de Saint Venant–Exner morphodynamic model. Adv. Water Resour. 113, 189–201.
Cordier, S., Le, M., Morales de Luna, T., 2011. Bedload transport in shallow water models: why splitting (may) fail, how hyperbolicity (can) help. Adv. Water Resour. 34, 980–989.
Del Gaudio, A., La Forgia, G., Constantinescu, G., De Paola, F., Di Cristo, C., Iervolino, M., Leopardi, A., Vacca, A., 2024. Modelling the impact of a dam-break wave on a vertical wall. Earth Surf. Process. Landf..
Di Cristo, C., Evangelista, S., Greco, M., Iervolino, M., Leopardi, A., Vacca, A., 2018. Dam-break waves over an erodible embankment: experiments and simulations. J. Hydraul. Res. 56, 196–210.
Di Cristo, C., Greco, M., Iervolino, M., Leopardi, A., Vacca, A., 2016. Two-dimensional two-phase depth-integrated model for transients over mobile bed. J. Hydraul. Eng. 142 (2), 04015043.
Di Cristo, C., Greco, M., Iervolino, M., Vacca, A., 2020. Interaction of a dam-break wave with an obstacle over an erodible floodplain. J. Hydroinform. 22, 5–19.
Di Cristo, C., Greco, M., Iervolino, M., Vacca, A., 2021. Impact force of a geomorphic dam-break wave against an obstacle: Effects of sediment inertia. Water 13, 232.
Fent, I., Zech, Y., Soares-Frazão, S., 2019. Dam-break flow experiments over mobile bed: velocity profile. J. Hydraul. Res. 57, 131–138.
Fraccarollo, L., Capart, H., 2002. Riemann wave description of erosional dam-break flows. J. Fluid Mech. 461, 183–228.
Goutiere, L., Soares-Frazão, S., Zech, Y., 2011. Dam-break flow on mobile bed in abruptly widening channel: experimental data. J. Hydraul. Res. 49, 367–371.
Graf, W.H., Altinakar, M.S., 1998. Fluvial Hydraulics: Flow and Transport Processes in Channels of Simple Geometry, vol. 42. Wiley, Chichester, New York.
Greco, M., Iervolino, M., Leopardi, A., 2008. Discussion of "divergence form for bed slope source term in shallow Water equations" by Alessandro Valiani and Lorenzo Begnudelli. J. Hydraul. Eng. 134, 676–678.
Heikkila, J., Silvén, O., 1997. A four-step camera calibration procedure with implicit image correction. In: Proceedings of IEEE Computer Society Conference on Computer Vision and Pattern Recognition. IEEE, pp. 1106–1112.
Juez, C., Murillo, J., García-Navarro, P., 2014. A 2D weakly-coupled and efficient numerical model for transient shallow flow and movable bed. Adv. Water Resour. 71, 93–109.
Lauber, G., Hager, W., 1998. Experiments to dambreak wave: Sloping channel. J. Hydraul. Res. 36, 761–773.
Leal, J.G., Ferreira, R.M., Cardoso, A.H., 2006. Dam-break wave-front celerity. J. Hydraul. Eng. 132, 69–76.
Liu, Y., Yang, C., Chen, X., 2022. Experimental study of bed morphology evolution under two-dimensional dam-break flow. J. Hydraul. Res. 60, 496–503.
Meyer-Peter, E., Müller, R., 1948. Formulas for bed-load transport. In: IAHSR 2nd Meeting, Stockholm, Appendix 2. IAHR.
Nikolos, I., Delis, A., 2009. An unstructured node-centered finite volume scheme for shallow water flows with wet/dry fronts over complex topography. Comput. Methods Appl. Mech. Engrg. 198, 3723–3750.
Soares-Frazao, S., Canelas, R., Cao, Z., Cea, L., Chaudhry, H.M., Die Moran, A., El Kadi, K., Ferreira, R., Cadórniga, I.F., Gonzalez-Ramirez, N., et al., 2012. Dam-break flows over mobile beds: experiments and benchmark tests for numerical models. J. Hydraul. Res. 50, 364–375.

Soares-Frazão, S., Le Grelle, N., Spinewine, B., Zech, Y., 2007. Dam-break induced morphological changes in a channel with uniform sediments: measurements by a laser-sheet imaging technique. J. Hydraul. Res. 45, 87–95.

Soares-Frazão, S., Zech, Y., 2011. HLLC scheme with novel wave-speed estimators appropriate for two-dimensional shallow-water flow on erodible bed. Internat. J. Numer. Methods Fluids 66, 1019–1036.

Spinewine, B., Capart, H., 2013. Intense bed-load due to a sudden dam-break. J. Fluid Mech. 731, 579–614.

Spinewine, B., Zech, Y., 2007. Small-scale laboratory dam-break waves on movable beds. J. Hydraul. Res. 45, 73–86.

Swartenbroekx, C., Zech, Y., Soares-Frazão, S., 2013. Two-dimensional two-layer shallow water model for dam break flows with significant bed load transport. Int. J. Numer. Methods Fluids 73 (5), 477–508.

The MathWorks Inc., 2022. MATLAB version: 9.13.0 (R2022b). URL: https://www.mathworks.com.

Wang, J.-S., Ni, H.-G., He, Y.-S., 2000. Finite-difference TVD scheme for computation of dam-break problems. J. Hydraul. Eng. 126 (4), 253–262.

Xu, T., Huai, W., Liu, H., 2023. MPS-based simulation of dam-break wave propagation over wet beds with a sediment layer. Ocean Eng. 281, 115035.

Yadav, A., Sen, S., Mao, L., Schwanghart, W., 2022. Evaluation of flow resistance equations for high gradient rivers using geometric standard deviation of bed material. J. Hydrol. 605, 127292.

Zh, Z., 2000. A flexible new technique for camera calibration. IEEE Trans. Pattern Anal. Mach. Intell. 22, 1330–1334.